ACS APPLIED MATERIALS & INTERFACES

www.acsami.org

Research Article

Size-Controlled Cu_3VSe_4 Nanocrystals as Cathode Material in Platinum-Free Dye-Sensitized Solar Cells

Chen-Yu Chang, Navdeep Kaur, Roberto Prado-Rivera, Cheng-Yu Lai, and Daniela Radu*

Cite This: *ACS Appl. Mater. Interfaces* 2024, 16, 13719−13728

Read Online

ACCESS | Metrics & More | Article Recommendations | Supporting Information

Downloaded via FLORIDA INTL UNIV on June 9, 2024 at 22:23:43 (UTC).
See https://pubs.acs.org/sharingguidelines for options on how to legitimately share published articles.

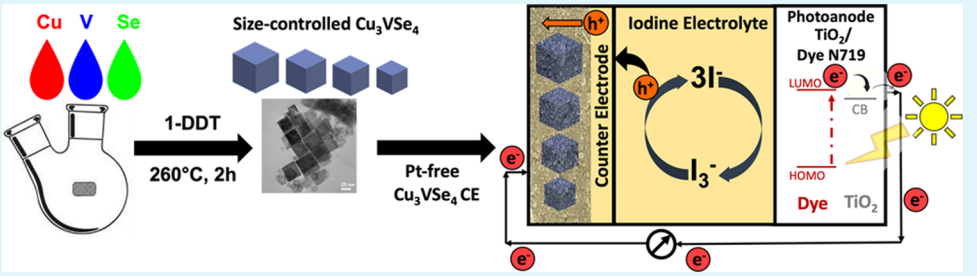

ABSTRACT: In this work, we report the first single-step, size-controlled synthesis of Cu_3VSe_4 cuboidal nanocrystals, with the longest dimension ranging from 9 to 36 nm, and their use in replacing the platinum counter electrode in dye-sensitized solar cells. Cu_3VSe_4, a ternary semiconductor from the class of sulvanites, is theoretically predicted to have good hole mobility, making it a promising candidate for charge transport in solar photovoltaic devices. The identity and crystalline purity of the Cu_3VSe_4 nanocrystals were validated by X-ray powder diffraction (XRD) and Raman spectroscopy. The particle size was determined from the XRD data using the Williamson−Hall equation and was found in agreement with the transmission electron microscopy imaging. Based on the electrochemical activity of the Cu_3VSe_4 nanocrystals, studied by cyclic voltammetry, the nanomaterials were further employed for fabricating counter electrodes (CEs) in Pt-free dye-sensitized solar cells. The counter electrodes were prepared from Cu_3VSe_4 nanocrystals as thin films, and the charge transfer kinetics were studied by electrochemical impedance spectroscopy. The work demonstrates that Cu_3VSe_4 counter electrodes successfully replace platinum in DSSCs. CEs fabricated with the Cu_3VSe_4 nanocrystals having an average particle size of 31.6 nm outperformed Pt, leading to DSSCs with the highest power conversion efficiency (5.93%) when compared with those fabricated with the Pt CE (5.85%).

KEYWORDS: *Cu_3VSe_4, Cu_3VSe_4 nanocrystals, sulvanite, nanocrystal size control, electrocatalytic activity, dye-sensitized solar cells*

1. INTRODUCTION

Resonant with rapidly rising global energy demands, renewable solar power harvesting, entailing low-cost, and ecofriendly power generation led to increased research efforts in the scientific community to reach commercially desired capabilities. Thus, significant photovoltaic (PV) technology advancements have been achieved in the past decade, hallmarked by the rise of third-generation solar photovoltaics, which showcases emerging materials, including organic molecules, halide perovskites, semiconductor quantum dots, and emerging solar cell architectures, including multiphoton harvesting and excitonic solar cell configurations. As part of this generation, dye-sensitized solar cells (DSSCs) have gained attention as an alternative to conventional silicon solar cells, mainly for their lower production cost, facile fabrication, and better operability in dim light conditions.[1] DSSCs consist of a photoanode made with mesoporous, nanocrystalline TiO_2, a light-absorbing dye, and a counter electrode (CE) made from a highly conductive and corrosion-resisted material.[2] Both the photoanode and the CE are deposited on the conductive substrate, typically fluorine-doped tin oxide (FTO) glass, and interact with an electrolyte solution, such as iodide/tri-iodide (I^-/I_3^-), in between. The CE plays an essential role in catalyzing the reduction of the electrolyte, transporting the photogenerated charge carriers from the electrolyte to the circuit. So far, platinum (Pt) has been considered the most performant CE material in DSSCs owing to its high electrocatalytic activity and excellent conductivity.[3] Despite these features, Pt is scarce and expensive, making it unfavorable for large-scale commercial manufacturing. Furthermore, Pt is prone to corrosion in iodide-based electrolytes, leading to PtI_4.[4,5] Extensive research to replace Pt as a CE has been conducted on various classes of materials; among these, carbonaceous materials (two-dimensional graphene, carbon black, and CNTs),[6,7] transition metal

Received: December 13, 2023
Revised: February 23, 2024
Accepted: February 26, 2024
Published: March 8, 2024

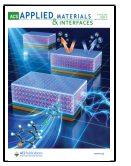

© 2024 American Chemical Society

https://doi.org/10.1021/acsami.3c18658
ACS Appl. Mater. Interfaces 2024, 16, 13719−13728

dichalcogenides[8] (MoS_2, SnS_2, WSe_2, and others), carbon−metal composites,[9,10] metal oxides (NiO, V_2O_5, and MoO_3),[11,12] and conductive polymer composites[13,14] were evaluated. In another approach, CuS/Graphene heterostructured nanocomposites were utilized as CE in DSSC. Despite demonstrating a 12% increase in power conversion efficiency (PCE), their standard photovoltaic performance was relatively inferior.[15] In this line, $Cu_2ZnSn(S,Se)_4$ popularly known as CZTSSe (Copper Zinc Tin Sulfo-Selenide) with nanosheet crystal morphology was also tested as an alternative for Pt-free DSSCs.[16]

Recently, a class of ternary copper chalcogenides, known as sulvanites (due to the parent compound, the sulvanite mineral Cu_3VS_4), has emerged and gained attention in the field of optoelectronics and energy storage due to its unique crystal structure, optical, and electronic properties.[17,18] The compounds in this class, with the general formula Cu_3MX_4 (M═V, Nb, or Ta; X═S, Se, or Te), possess band gaps ranging from 1.3 to 2.8 eV (depending on the chemical composition) within the range of interest for optoelectronics; in addition, several sulvanite compounds exhibit *p*-type conductivity, with high carrier mobility.[19,20] As a result, the sulvanite compounds have been used in various fields such as photovoltaics, hydrogen evolution catalysis, laser protection, and various battery technologies (sodium-ion, potassium-ion, and lithium-ion).[21−27] In addition to their electronic properties, sulvanites containing Cu and V benefit from the Earth abundance of these elements, making them sustainable.

While the fundamental material properties of the sulvanites, including optical, electronic, and vibrational,[19,28−31] have been known for decades, their applications started to emerge after their synthesis at the nanoscale, provided that the bulk materials, obtained typically through solid-state synthesis at high temperatures and long reaction times,[32,33] consist of large-sized crystals. Recently, the first synthesis of nanocrystalline Cu_3VS_4 was reported, and it was achieved through colloidal synthesis.[34] Unlike the solid-state route, the colloidal approach enables fine control over the size of the nanocrystal, which further opens the window for size-dependent properties provided by quantum confinement.[35,36] For example, Mantella et al. demonstrated the size-dependent optical properties of Cu_3VS_4 nanocrystals by tuning the reaction temperature.[24] The synthesis of nanoscale sulvanites with various morphologies and compositions followed.[17,37,38] The synthesized colloidal nanocrystals not only benefit from facile and expeditious synthesis but, most importantly, enable stable dispersions, which are critical to thin film and device fabrication.

Considering the demand for low-cost, Earth-abundant, and high-performance CE materials, Cu_3VSe_4 (CVSe) was selected due to the abundant elements in its composition, relatively high carrier mobility, and excellent electrochemical performance.[19,39] This work reports the first single-step colloidal synthesis method for CVSe nanocrystals. In contrast to previous reports,[40] we show that particle size can be controlled by tailoring the amount of the added surfactant. The purity of the CVSe nanocrystals was confirmed by X-ray diffraction (XRD) and Raman spectroscopy. The crystallite size as a function of the amount of added surfactant was estimated by using the Williamson−Hall method applied to the XRD data and further validated by transmission electron microscopy (TEM). The optical absorbance of the nanocrystals was measured by ultraviolet−visible (UV−vis) spectroscopy. CVSe/FTO CEs were prepared by spin-coating the obtained CVSe nanocrystal dispersions onto FTO substrates. Scanning electron microscopy (SEM) and atomic force microscopy (AFM) were used to verify the film quality. The thickness of the CVSe film was determined by cross-sectional SEM imaging. Finally, the Pt-free DSSC PV performance of the CVSe/FTO CE fabricated from various CVSe nanocrystal sizes was investigated. The cell's performance was explained through the charge transport kinetics observed from the electrochemical impedance spectroscopy (EIS) measurements relating to the electrocatalytic activity obtained from the cyclic voltammetry (CV) curves and the conductivity measurements.

2. METHODS

2.1. Reagents. Vanadium(IV) oxide acetylacetonate ($VO(acac)_2$, ≥98%) was ordered from Merck KGaA. Chloroform ($CHCl_3$, 99.9%, Fisher), copper(I) chloride (CuCl, 99%, Sigma-Aldrich), 1-dodecanethiol (1-DDT, 98%, Aldrich), ethanol (EtOH, anhydrous, Decon), selenium powder (Se, 99.99%, Aldrich), oleylamine (OLA, 70%, Aldrich), and methyl acetate (MeOAc, anhydrous, 99.5%, Sigma-Aldrich) were all used as received, without further purification. For PV device fabrication, the following were purchased: fluorine-doped tin oxide (FTO) substrates from Hartford Glass Co., Inc.; zinc powder, titanium(IV) isopropoxide (TTIP), titanium dioxide (TiO_2) paste, lithium iodide (LiI), lithium perchlorate ($LiClO_4$), and iodine (I_2) from Sigma-Aldrich (Saint Louis, MI); Platisol-T from Solaronix (Aubonne, CH); ditetrabutylammonium *cis*-bis(isothiocyanato)bis-(2,2′-bipyridyl-4,4′-dicarboxylato) ruthenium(II) (N719) dye and EL-HSE electrolyte from Greatcell Solar Co. Ltd. (Queanbeyan, AU).

Note. Standard Schlenk line techniques were used for all of the syntheses. Inhalation of chemicals can cause serious health problems; therefore, it is recommended to perform all synthetic steps in a fume hood, wearing appropriate personal protective equipment.

2.2. Preparation of Cu_3VSe_4 Nanocrystal Dispersions and Spin-Coated Films. The standard Schlenk line technique was used in all syntheses. CuCl (2.2 mmol, 220 mg), $VO(acac)_2$ (1 mmol, 265 mg), Se (3 mmol, 240 mg), and OLA (20 mL) and predetermined amounts of 1-DDT (0, 0.25, 0.5, and 0.75 mL) were loaded into a 250 mL round-bottom flask. Next, the mixture was degassed at 120 °C under vacuum for 30 min. After the degassing, the temperature was increased to 260 °C, and the reaction was conducted for 2 h under stirring. Afterward, the reaction was allowed to cool naturally, followed by the purification steps. The nanoparticles were washed three times by using a $CHCl_3$/EtOH solvent pair and collected each time by centrifugation. A postsynthesis ligand exchange was conducted to replace the long alkyl-chain OLA and 1-DDT ligands originating from the synthesis with short-chain methyl acetate (MeOAc). This step is designed to improve the electrical conductivity by reducing the nonconductive long alkyl-chain hydrocarbons attached to the surface of the nanocrystals. Thirty milliliters of MeOAc was added to the obtained nanoparticle dispersion, followed by centrifugation. The final dispersion to be utilized in thin film fabrication ("ink") is prepared by redispersing the precipitate in 10 mL of $CHCl_3$.

2.3. Device Fabrication. The DSSC device fabrication steps were adopted from our previous work;[41−43] the photoanodes and the counter electrodes were prepared separately, which were then assembled and followed by an insertion of I^-/I_3^- electrolyte (60 μL) in between. The preparation steps for individual photoanodes and CEs are as follows:

2.3.1. Photoanode Preparation. Photoanodes were prepared from a mesoporous TiO_2 (m-TiO_2) layer doctor-bladed onto spray-coated compact TiO_2 (c-TiO_2) on patterned FTO substrates. The patterning of the FTO substrates was performed via chemical etching, where zinc paste was deposited on the FTO layer, etched with aqueous HCl (18.5% v/v) added dropwise, and then rinsed copiously with nanopure water. Next, the patterned substrates were thoroughly cleaned by ultrasonication in the following process: (1) a soap solution of Hellmanex III in nanopure water (2% v/v), (2) nanopure

https://doi.org/10.1021/acsami.3c18658
ACS Appl. Mater. Interfaces 2024, 16, 13719−13728

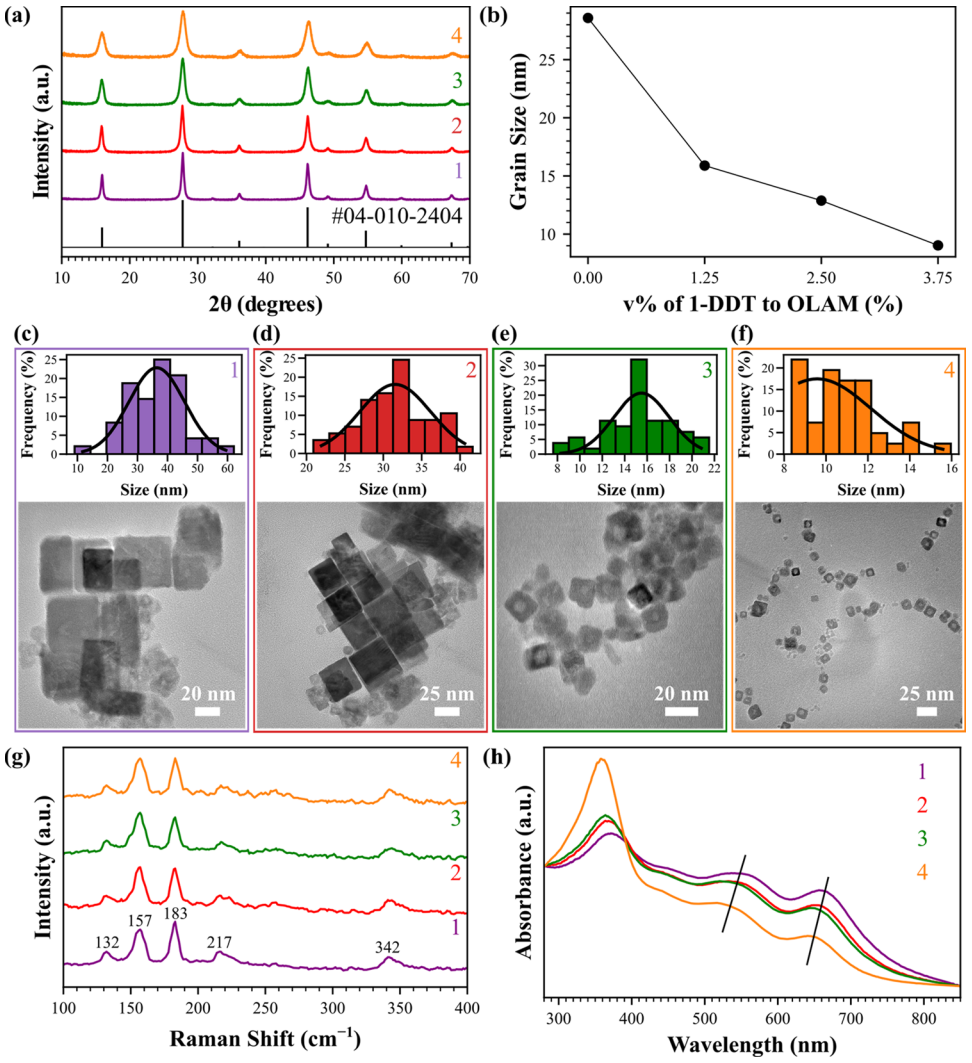

Figure 1. (a) XRD results of the synthesized CVSe nanocrystals with different amounts of 1-DDT added. The reference pattern of CVSe was obtained from the ICDD database. (b) The estimated crystallite size derived from the Williamson−Hall plots. (c−f) Low-magnification TEM images of the CVSe nanocrystals and their size distribution. (g) Raman spectra of the CVSe nanocrystals. (h) UV−vis absorbance spectra of the CVSe nanocrystals. The labels #1, #2, #3, and #4 denote 0, 0.25, 0.5, and 0.75 mL of added 1-DDT, corresponding to particle sizes of 36.26, 31.62, 15.20, and 10.87 nm, respectively.

water, (3) acetone, (4) ethanol, and (5) isopropanol heated to 80 °C; at each step, the substrates were ultrasonicated for 15 min and dried with the nitrogen flow. After cleaning, the FTO substrates were treated with an Ossila UV ozone cleaner for 30 min to remove any remaining organic surface contaminants. The treated FTO substrates are placed onto a hot plate for several minutes until they reach a target temperature of 450 °C. Once the substrates met the target temperature, a layer of c-TiO2 was deposited on the heated substrates by spraying a 0.4 M solution of TTIP in ethanol and keeping it there for 30 min before being cooled to room temperature. A layer of m-TiO_2 (effective area of 0.15 cm^2) was then doctor-bladed on top of the freshly prepared c-TiO_2 layer. The m-TiO_2/c-TiO_2/FTO substrate was annealed at 450 °C for 1 h. The thickness of m-TiO_2 was observed to be 11.5 μm obtained from cross-sectional SEM, performed as reported in our previous work.[44] Finally, the m-TiO_2/c-TiO_2/FTO substrate was soaked in 0.4 mM of N719 dye solution in ethanol for 20 h. Figure S1 depicts the images of the patterned FTO, before and after dye-loaded m-TiO_2/c-TiO_2/FTO.

2.3.2. Counter Electrode Preparation. A Pt reference CE is prepared by drop-casting 60 μL of Platisol-T onto precleaned FTO substrates (see Photoanode preparation) and annealed at 450 °C for 30 min. To obtain CVSe CEs, CVSe dispersions of varying particle sizes are first prepared by dispersing ligand-exchanged CVSe nanocrystals in 10 mL of $CHCl_3$, forming an opaque black solution. These dispersions were then spin-coated onto precleaned FTO substrates at 500 rpm for 30 s, forming a CVSe film. The CVSe film/FTO substrate is annealed at 120 °C in the air for 10 min, evaporating any remaining solvent.

2.4. Characterization. X-ray diffraction (XRD) was performed on a Rigaku MiniFlex with a Cu-Kα radiation source (λ = 1.5405 Å) and operated at 40 mV and 30 mA. Crystallite size analysis was conducted using the Williamson−Hall equation. Raman measurements were conducted on a WITec α 300 Raman microscope with a 532 nm laser. Transmission electron microscope (HR-TEM) images were obtained on JEOL JEM-2100 Plus with a 200 kV LaB_6 electron source. TEM samples were prepared by dropping dilute dispersions of each nanoparticle batch onto Au TEM grids. Scanning electron microscope (SEM) images were collected using a JEOL/JSM-F100 Schottky field emission SEM equipped with an energy-dispersive X-ray spectroscopy detector (SEM/EDX). Fourier transform infrared spectroscopy (FT-IR) was conducted on a Shimadzu/IRTracer-100 instrument with an attenuated total reflectance (ATR) attachment. UV−vis−NIR measurements were conducted by using a Shimadzu UV-3600 Plus spectrophotometer. Atomic force microscopic (AFM) images were obtained on an Anton Paar Tosca 400 AFM. Photovoltaic (PV) cell testing was performed with an ORIEL LCS-100TM solar simulator

https://doi.org/10.1021/acsami.3c18658
ACS Appl. Mater. Interfaces 2024, 16, 13719−13728

under one sun illumination (1.5 G AM) at an incident power intensity of 100 mW cm^{-2}. The solar simulator was calibrated with a silicon solar cell for data accuracy. Electrochemical impedance spectroscopy (EIS) measurements of the fabricated DSSCs were performed immediately after the $J-V$ measurements using an Ω Metrohm Autolab instrument. The measurements were conducted by connecting the FTO part of the photoanode and CE to the Autolab instrument using a two-electrode electrochemical setup. During EIS measurement, the fabricated DSSCs were exposed to one sun illumination (1.5 G AM) at an incident power intensity of 100 mW cm^{-2}. EIS measurements for each cell were taken at their respective V_{OC}, obtained from the $J-V$ curves, while maintaining a frequency range of 0.1 Hz to 1 MHz. Cyclic voltammetry (CV) measurements were performed using the same instrument, employing a three-electrode system. The three-electrode system included a Pt counter electrode, a Ag/AgCl reference electrode, and the target sample (Pt or CVSe) on the FTO substrate as the working electrode. All three electrodes were immersed in an electrolyte containing $LiClO_4$ (0.1 M), I_2 (1 mM), and LiI (10 mM) in an acetonitrile solution at room temperature. CV data for the Pt and CVSe films on FTO were collected within the voltage range of −1 to 1.5 V, starting and stopping potential at 0 V, and a scan rate of 50 $mV{\cdot}s^{-1}$. A stabilization time of 5 s was maintained before recording the CV data. Electrical conductivity was measured by using an Ossila T2001A3 four-point probe station.

3. RESULTS AND DISCUSSION

3.1. Nanocrystal Synthesis and Characterization. Cu_3VSe_4 nanocrystals were prepared through a simple single-step synthesis known as the "heat-up" or "one-pot" method.[45] In this method, precursors are mixed and then heated at a controlled rate to facilitate nucleation. This method is easy to operate and can be readily scaled up for mass production compared to other colloidal methods. More importantly, this method drastically minimizes the user-to-user differences reported using the "hot injection" method, where precursors are added to the mixture at various stages throughout the synthesis.[37,38,46,47] We found that 1-DDT can be used as a strong capping ligand for size control owing to its strong affinity to selenium.[48] Three 1-DDT to OLA volume ratios (v:v) have been used: 1.25, 2.5, and 3.75, respectively (0.25, 0.5, and 0.75 mL using a fixed amount of OLA, 20 mL), along with a control experiment with no 1-DDT addition. All other reaction parameters, including chemical reagents, reaction time, and reaction temperature, were kept the same. Powder XRD was utilized to confirm the purity of the obtained nanocrystals. The diffraction patterns of all samples matched closely with the database reference (ICDD #04-010-2404, cubic, $P\bar{4}3m$ space group), as shown in Figure 1a. A pronounced peak broadening effect, characteristic of nanomaterials, can be observed from the diffraction patterns; lower 1-DDT:OLA volume ratio samples present sharp and narrow peaks, while higher ones yield lower intensities and broader peaks. This peak broadening effect was further examined by estimating the average crystallite sizes using the Williamson−Hall equation, and the results are shown in Figure 1b and the Williamson−Hall plots can be found in Figure S2. The addition of 1-DDT can effectively reduce the crystallite size: when no 1-DDT was added, the crystallite size is estimated to be around 28 nm, while in different amounts of added 1-DDT (0.25 0.5, and 0.75 mL), the average crystallite size decreased to 15.89, 12.88, and 9.03 nm, respectively. This decreasing trend with respect to the added 1-DDT amounts also extends to particle size, as visually confirmed by low-magnification TEM images and corresponding particle size distributions (Figure 1c−f). These results are summarized in Table 1. The crystallite size is generally smaller than the particle size for all concentrations, indicating the polycrystalline nature of the CVSe nanocrystals. At higher 1-DDT:OLA ratios, the difference between crystallite and particle size becomes smaller, indicative of the 1-DDT potential contribution to single crystal synthesis.

Table 1. Comparison of Crystallite Size from the Williamson−Hall Equation and TEM for the Four Different Experimental Conditions

sample	added 1-DDT (mL)	1-DDT:OLA (v:v)	crystallite size (nm)	particle size (nm)
#1	0	0	28.58	36.26 ± 9.13
#2	0.25	1.25	15.89	31.62 ± 4.60
#3	0.5	2.5	12.88	15.2 ± 3.00
#4	0.75	3.75%	9.03	10.87 ± 1.73

Raman spectroscopy indicates that regardless of the 1-DDT:OLA ratio, all samples possess identical spectra and have five distinguishable peaks positioned at 132, 157, 183, 217, and 342 cm^{-1}, respectively, which is consistent with the values reported before.[38,40] The two peaks at 132 and 342 cm^{-1} can be attributed to the F_2^a and F_2^d vibrational modes of the Cu_3VSe_4 crystal as suggested by the computational work,[30,49] as Raman information is scarce in literature for this compound. Figure 1h shows the UV−vis spectra obtained from the nanoparticle dispersions. All samples generally exhibit three absorption peaks at around 378, 548, and 663 nm, with the first peak having the strongest absorption. As the particle size decreases, significant blue shifting can be observed, as previously reported for Cu_3VS_4 nanocrystals, and the values can be found in Table S1 (Supporting Information).[36] High-magnification TEM imaging of an isolated CVSe nanocrystal is shown in Figure 2, which shows highly crystalline cuboidal nanocrystals with continuous lattice fringes throughout the entire particle. The d-spacing was measured to be 0.57 nm, which can be assigned to the (100) plane of CVSe according to the ICDD reference.

For better performance in Pt-free DSSCs, a high-quality film with a large contact area is essential to facilitate electrochemical reactions. SEM and AFM imaging were used to examine the quality of the deposited CVSe #2 film on the FTO. The top-view SEM image (Figure 3a) shows a uniform film of cuboidal CVSe nanocrystals, consistent with the TEM images. The 10 × 10 μm AFM topography in Figure 3b has a calculated RMS roughness of around 73 nm. The thickness of the deposited CVSe layer was measured to be approximately 500 nm from the SEM cross-sectional image, as shown in Figure 3c. The same thickness has been maintained for CVSe #1, #2, #3, and #4 films by ensuring consistent preparation conditions and spin-coating parameters. Figure 3d shows the cross-sectional SEM-EDX mapping of the CVSe film on top of the FTO substrate, revealing a uniform distribution of all of the elements across the layer. The atomic ratio of the CVSe layer was calculated to be 2.5/1.2/4 (Cu/V/Se) based on the EDX spectrum (Figure S3).

3.2. Cyclic Voltammetry and Conductivity Measurements. The electrocatalytic activity of the fabricated CVSe films was investigated by cyclic voltammetry (CV) measurements. The CV measurements were conducted on a three-electrode system using Pt (counter electrode), Ag/AgCl

https://doi.org/10.1021/acsami.3c18658
ACS Appl. Mater. Interfaces 2024, 16, 13719−13728

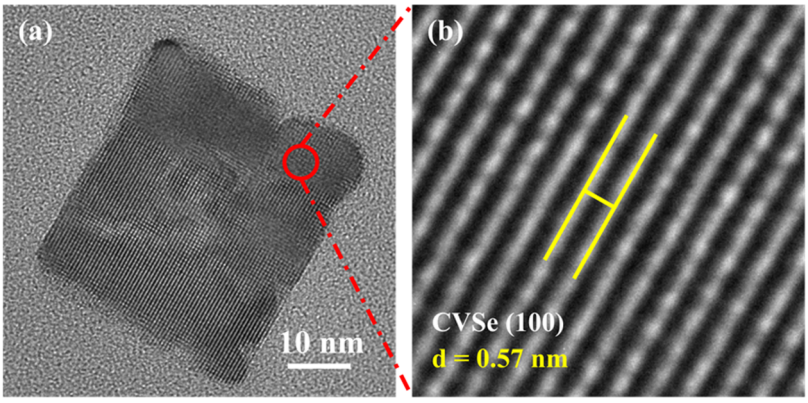

Figure 2. (a) High-magnification TEM image of an isolated CVSe cuboid (sample #2). (b) Lattice fringes of the same particle show a *d*-spacing of 0.57 nm, attributed to the (100) plane.

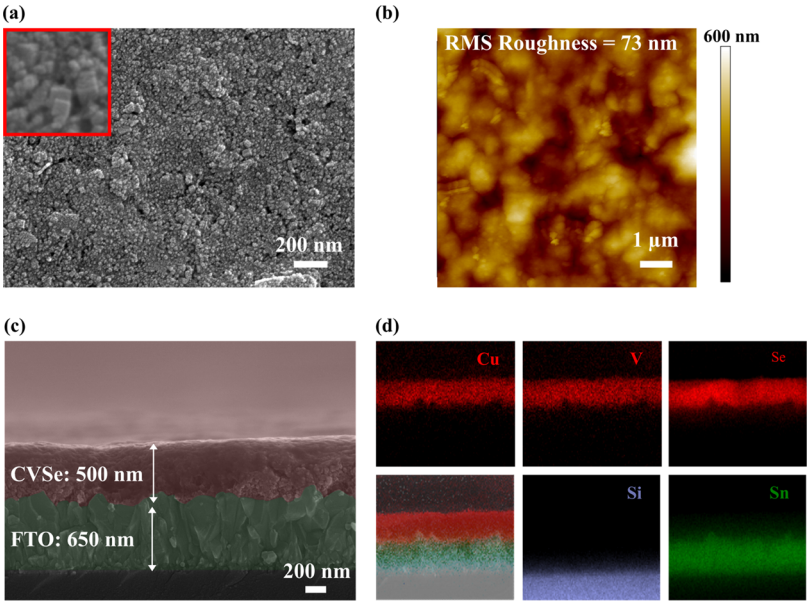

Figure 3. (a) Top-view SEM image of a spin-coated #2 CVSe film. (b) AFM topography of the spin-coated #2 CVSe film. (c) Cross-sectional SEM and (d) cross-sectional SEM-EDX mapping of the spin-coated #2 CVSe film on FTO substrate.

(reference electrode), and a working electrode (Pt and CVSe thin films). The working electrode was immersed in an electrolyte containing $LiClO_4$ (0.1 M), I_2 (1 mM), and LiI (10 mM) in an acetonitrile solution. As shown in Figure 4a, positive oxidation and negative reduction peaks can be observed, which can be attributed to the reactions described by the eqs 1 and 2:[50]

$$I_3^- + 2e^- \leftrightarrow I^- \quad (1)$$

$$3I_2 + 2e^- \leftrightarrow 2I_3^- \quad (2)$$

The electrocatalytic performance of the electrode can be determined by two key parameters: the reduction peak current density (J_{PC}) and the difference between reduction and oxidation peaks (ΔE_{PP}) on the CV curves.[5,51−53] For optimal electrocatalytic activity, the electrode must exhibit a high J_{PC} with simultaneously small E_{PP} values. The J_{PC} and ΔE_{PP} values of each CE are summarized in Table 2. The Pt CE exhibited two oxidation and reduction peak pairs, whereas the CVSe electrodes showed one oxidation and reduction peak pair. The J_{PC} values of the CVSe electrodes are comparatively higher than that of the Pt CE, along with a shift in the reduction peak potentials (E_{PC}) toward more negative potentials, resulting in comparatively larger ΔE_{PP} values. This increase in the J_{PC} values can be attributed to more available active sites on the CVSe electrodes resulting from the material's nanocrystal morphology. These larger ΔE_{PP} values for the CVSe CE than for the Pt CE might be attributed to the thickness and adhesion of the films, resulting in higher overpotential losses. The general trend in the CVSe CEs is that the J_{PC} increases between CEs #1 and #2 before decreasing in CEs #3 and #4 (inset of Figure 4a), while ΔE_{PP} increases as the particle size decreases. The lower J_{PC} value for the larger CVSe particle size (36.26 nm (no. 1)) could be correlated with the comparatively lesser number of electrocatalytic active sites on larger-sized particles. In the case of smaller particle sizes (15.2 nm (#3), 10.87 nm (#4)), although they have larger electrocatalytic active sites, the conductivity is significantly reduced, resulting in lower peak currents. While the ΔE_{PP} for Pt is smaller than that of #2 CVSe, a significant increase in the J_{PC} value of the latter could have possibly counterbalanced its electrocatalytic action. Hence, among the different particle-sized CVSe CEs and Pt CE, #2 CVSe exhibited better electrocatalytic activity toward the I^-/I_3^- redox electrolyte. Based on these results, we

https://doi.org/10.1021/acsami.3c18658
ACS Appl. Mater. Interfaces 2024, 16, 13719−13728

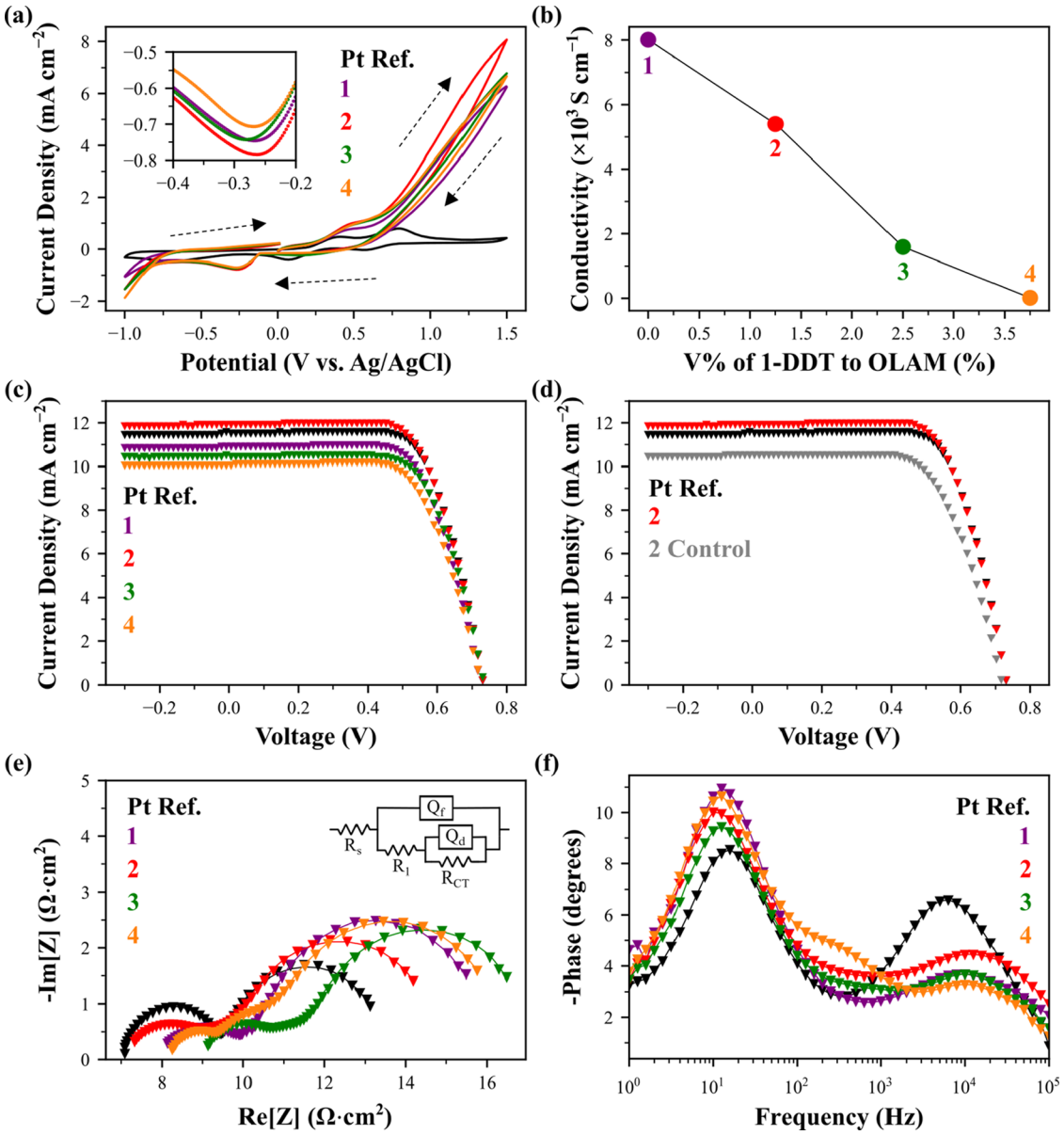

Figure 4. (a) Cyclic voltammetry curves of a reference Pt and CVSe CEs. (b) Electrical conductivity measurements of the CVSe films on FTO substrates via the four-point probe method. (c) $J-V$ curves of the fabricated DSSC devices using Pt CE (Pt ref) and CVSe nanocrystal CEs with varying sizes. (d) $J-V$ curves of sample #2 with and without MeOAc post-treatment. (e) Nyquist plots with the fitted circuit and (f) Bode plots of fabricated Pt-free DSSCs using CVSe CEs. The labels #1−#4 denote CVSe nanoparticle sizes of 36.3, 31.6, 15.2, and 10.9 nm, respectively.

Table 2. Measured Electrochemical and PV Performances of the Fabricated DSSCs Were Performed Using Pt and CVSe CEs[a]

counter electrode	$\lvert J_{PC}\rvert$ (mA·cm^{-2})	ΔE_{PP} (V)	J_{SC} (mA·cm^{-2})	V_{OC} (V)	FF	PCE (%)
Pt reference	0.408	0.336	11.51	0.73	0.69	5.85 ± 0.03
#1	0.746	0.757	10.91	0.72	0.68	5.38 ± 0.034
#2	0.786	0.767	11.92	0.73	0.68	5.93 ± 0.02
#2 control			10.53	0.72	0.64	4.85 ± 0.04
#3	0.743	0.817	10.14	0.74	0.69	5.26 ± 0.05
#4	0.704	0.814	9.47	0.74	0.69	4.92 ± 0.15

[a] $\lvert J_{PC}\rvert$ is the reduction peak current density, ΔE_{PP} is the difference between reduction and oxidation peaks, J_{SC} is the short-circuit current density, V_{OC} is the open circuit voltage, FF is the fill factor, and PCE is the power conversion efficiency.

hypothesized that #2 CVSe will perform comparably to a Pt CE in DSSCs.

Besides electrochemical activity, electrical conductivity is another critical parameter to consider when selecting a CE material for DSSCs. Electrical conductivity measurements were conducted on the CVSe/FTO instrument using a four-point probe station, as shown in Figure 4b. The result indicates that the electrical conductivity of CVSe films reduces as the particle size decreases. We posit that the reduction in electrical conductivity is caused by the long-chain hydrocarbon residuals

https://doi.org/10.1021/acsami.3c18658
ACS Appl. Mater. Interfaces 2024, 16, 13719−13728

on the surface of the CVSe nanocrystals.[54] To confirm this hypothesis, FT-IR was used to characterize the amount of hydrocarbon remaining on the CVSe film surfaces (Figure S4). The result shows that the small-sized CVSe samples present significantly higher absorption at $\nu_{as}(CH_3)$ = 2920 and $\nu_{as}(CH_2)$ = 2850 cm^{-1}, indicating higher amounts of hydrocarbon presence.

3.3. CVSe Particle Size Effect Investigations on the Photovoltaic Performance of Pt-Free DSSC. The photocurrent density−voltage ($J-V$) in Figure 4c shows the performance of the DSSCs fabricated with a reference Pt CE and other CVSe CEs (#1, #2, #3, and #4) with the parameters derived from the $J-V$ curve tabulated in Table 2. The cells using the #2 CVSe CE show the best PCE of 5.93%, which outperforms the reference cell with the Pt CE (5.85%) and other CVSe-based CEs. This could be attributed to the comparatively superior electrocatalytic activity of #2 CVSe CE, concurrently exhibiting the highest J_{PC} value obtained from CV curves and hence the highest J_{SC} value among all of the tested CEs in DSSCs. The comparatively poor photovoltaic performance of #1 CVSe CE DSSC is attributed to its deficient electrocatalytic action, leading to a lower J_{SC} value. Furthermore, with a decrease in the particle size of CVSe #3 and #4, the J_{SC} of the respective DSSCs significantly drops due to their comparatively poor electrical conductivity, indicating poor charge collection efficiency at the CE/electrolyte interface, thus leading to poor DSSC performance. Not only does the J_{SC} drop in #3 and #4 CVSe CE DSSCs, but the FF also decreases, which could be attributed to the easy miscibility of the CVSe films made of smaller particles in the I^-/I_3^- electrolyte medium. To assess the efficacy of novel CVSe nanocrystals in Pt-free DSSCs, the research findings related to Pt-free DSSCs employing various materials as CEs are summarized in Table S2 (Supporting Information).

To understand if the nanoparticle's postsynthesis processing via ligand exchange ultimately impacts the performance of the CVSe CEs, a control experiment was conducted by fabricating the DSSCs with CVSe films (#2) without the MeOAc postprocessing. MeOAc is commonly used in colloidal synthesized perovskite quantum dots as a short-chain ligand.[55] As demonstrated in Figure 4d, the control group without postprocessing exhibits a lower J_{SC}, leading to a lower PCE than the ones that underwent the MeOAc post-treatment. This control study highlights the importance of MeOAc post-treatment to improve the performance of CVSe CEs.

For DSSC device fabrication, three Pt CE and three CVSe CEs for each particle size (a total of 12 Pt-free devices) were fabricated. The fabrication was repeated six times for each cell configuration. Figure 5 shows the reproducibility of all of the fabricated DSSCs. Batch-to-batch reproducibility of fabricated DSSCs with Pt reference and CVSe#2 CE is represented in Figure S5.

3.4. Understanding Charge Transfer Kinetics in Pt-Free DSSCs via Electrochemical Impedance Spectroscopy. Electrochemical impedance spectroscopy (EIS) studies were conducted to elucidate the charge transfer kinetics at the different interfacial layers of the DSSCs. Figure 4e shows the Nyquist plot of the fabricated DSSCs utilizing CVSe CEs, from which two semicircles can be observed. The diameter of the first small semicircle at the higher frequency represents the charge transfer resistance at the CE/electrolyte interface (R_{CT}), and its x-intercept represents the series resistance (R_S) of the device. The diameter of the second semicircle in the lower

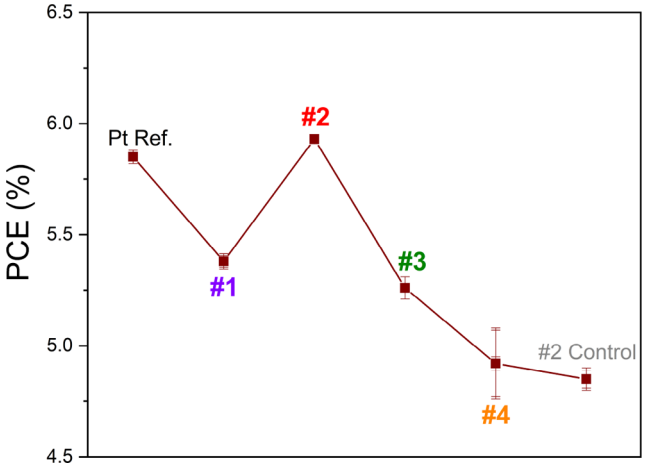

Figure 5. Reproducibility of Pt CE and #1, #2, #3, and #4 CVSe CE-based DSSC in one batch along with error bars.

frequency region represents the charge transfer resistance at the photoanode/electrolyte interface (R_1). The comparatively lower R_{CT} values of the CVSe CEs than Pt CE indicate faster photogenerated electron charge transfer from CE to the electrolyte, resulting from the redox capability of the former CVSe films. Further, a decreasing trend in the R_{CT} values from #1 to #4 CVSe CEs is observed. Although R_{CT} decreased at #3 and #4 CVSe CEs, the simultaneous increased R_1 value restricts the charge transportation throughout DSSCs and hence reduces their PV performance. Moreover, the smaller R_{CT} of CVSe CEs indicates faster dye molecule regeneration via oxidation reactions occurring at the CE/electrolyte interface. Furthermore, the R_S values of CVSe CEs are larger than those of Pt CE, which might be due to the comparatively lower conductivity of the CVSe compared to Pt. The obtained EIS parameters R_S, R_{CT}, and R_1 for all of the fabricated DSSCs are tabulated in Table 3. CE #2 exhibits the smallest R_1 among

Table 3. EIS Parameters of DSSCs Were Obtained with Pt and Cu_3VSe_4 CEs

counter electrode	R_S (Ω cm^2)	R_{CT} (Ω cm^2)	R_1 (Ω cm^2)	τ (μs)
reference	7.09	2.34	3.91	25.20
#1	8.13	1.81	5.58	15.92
#2	7.33	1.73	5.53	12.65
#3	9.16	1.65	5.86	15.92
#4	8.33	1.06	6.57	16.66

the CVSe CEs, indicating improved photogenerated electron transport at the photoanode/electrolyte interface.[56] It might be due to the relatively faster regeneration of dye molecules through oxidation reactions in the electrolyte medium. Considering the accelerated redox reactions in the electrolyte medium due to the superior electrocatalytic activity of CVSe CEs, the N719 dye undergoes regeneration facilitated by the I^- ions from the redox electrolyte. This regeneration process indirectly results in a reduced number of excited dye molecules, compelling the photogenerated charge carriers to transport toward m-TiO_2 instead of undergoing recombination within the N719 dye. Additionally, for CVSE #4 CE DSSCs, a new semicircle emerges between the first and second semicircles, unlike Pt, #1, #2, and #3 CVSe CEs in DSSCs. This phenomenon is a common characteristic of highly porous materials used as CEs.[57] The particle size of #4 CVSE has

https://doi.org/10.1021/acsami.3c18658
ACS Appl. Mater. Interfaces 2024, 16, 13719−13728

significantly reduced to 10.87 nm, indicating a high probability of increased porosity, which, in turn, leads to the presence of the new semicircle.

To further establish a correlation between the better electrocatalytic activity and PV performance of CVSe CE, the photogenerated electron lifetime at the CE/electrolyte interface is estimated from the Bode plots (Figure 4f). The Bode plot shows two peaks at lower and higher frequencies corresponding to the photoanode/electrolyte and CE/electrolyte interface, respectively. It is evident that the frequency maxima (f_{max}) of the high-frequency peak of CVSe CEs shift to a higher frequency, thus resulting in a shorter photogenerated electron lifetime (τ) in Pt-free DSSCs as calculated from the following equation

$$\tau = \frac{1}{2\pi f_{max}} \quad (3)$$

It is observed that CE #2 exhibited the shortest τ value among the Pt, #1, #3, and #4 CE DSSCs, indicating better charge transfer kinetics at photoanode/electrolyte and CE/electrolyte interfaces, and the results agree with its higher PV performance and better electrocatalytic action.

Hence, for the first time, Cu_3VSe_4 sulvanites with a nanocuboid morphology were proven to be an effective alternative to fabricating cost-effective, high-performing Pt-free DSSCs via low-temperature fabrication conditions, paving the way for use in any thin film optoelectronics and solar photovoltaics, including perovskite solar cells or quantum dot solar cells.

4. CONCLUSIONS

A facile synthesis of size-controlled cuboid Cu_3VSe_4 nanocrystals in one step was successfully conducted and exemplified for four different nanocrystal sizes. The major finding of the reported synthesis work is that the size of the Cu_3VSe_4 cuboid nanocrystals can be tailored as a function of the employed surfactant ratio. The purity of the synthesized nanocrystals was validated by XRD and Raman spectroscopy. The crystallite and nanoparticle sizes were estimated using the Williamson−Hall equation and TEM, respectively. The electrochemical characterization of Cu_3VSe_4 suggested their potential for application in solar photovoltaics. In this line, Cu_3VSe_4 nanocrystal dispersions were deposited by spin-coating onto FTO substrates, and the obtained thin films were utilized as counter electrodes to construct Pt-free DSSCs. The study revealed that the calculated PCE of the DSSCs is dependent on the particle sizes of the Cu_3VSe_4 films. An impressive PCE of 5.93% was calculated for the Cu_3VSe_4 CE fabricated with the particles having a 31.6 nm average particle size, outperforming the other Cu_3VSe_4 CEs and the Pt reference (5.85%). This higher PCE is attributed to the balanced electrocatalytic activity and the electrical conductivity of the Cu_3VSe_4 electrodes, for which the CE exhibited better electrocatalytic activity among other CEs. The electrical conductivity of the Cu_3VSe_4 electrodes is primarily hindered by the residual hydrocarbon on the surface of the particles, especially when affecting smaller particles. Therefore, although a smaller particle size is beneficial for providing more active sites for electrocatalytic activity, the amount of unremovable hydrocarbon residuals must also be considered. Moreover, performant Cu_3VSe_4 exhibited enhanced charge transport kinetics, supported by EIS measurements. This comprehensive study of Cu_3VSe_4 nanocrystal synthesis, characterization, and Pt-free DSSC testing provides grounds for the application of other nanoscale sulvanites in DSSCs as well as other applications in optoelectronics and thin-film semiconductor electronics.

ASSOCIATED CONTENT

Supporting Information

The Supporting Information is available free of charge at https://pubs.acs.org/doi/10.1021/acsami.3c18658.

Image of the photoanode; UV−vis peak values; Williamson−Hall plots; SEM-EDX spectrum of the CVSe on an FTO substrate; FT-IR of the CVSe CEs; reproducibility of the DSSCs; comparison of PV performance of other Pt-free DSSCs having I^-/I_3^- electrolyte medium (PDF)

AUTHOR INFORMATION

Corresponding Author

Daniela Radu − *Department of Mechanical and Materials Engineering, Florida International University, Miami, Florida 33174, United States;* orcid.org/0000-0001-6833-5825; Email: dradu@fiu.edu

Authors

Chen-Yu Chang − *Department of Mechanical and Materials Engineering, Florida International University, Miami, Florida 33174, United States;* orcid.org/0000-0001-5253-1813

Navdeep Kaur − *Department of Mechanical and Materials Engineering, Florida International University, Miami, Florida 33174, United States;* orcid.org/0000-0002-4140-1535

Roberto Prado-Rivera − *Department of Mechanical and Materials Engineering, Florida International University, Miami, Florida 33174, United States;* orcid.org/0000-0002-3376-6673

Cheng-Yu Lai − *Department of Mechanical and Materials Engineering, Florida International University, Miami, Florida 33174, United States; Department of Chemistry and Biochemistry, Florida International University, Miami, Florida 33199, United States;* orcid.org/0000-0002-8931-5601

Complete contact information is available at: https://pubs.acs.org/10.1021/acsami.3c18658

Author Contributions

The manuscript was written through the contributions of all authors. All authors have given approval to the final version of the manuscript.

Notes

The authors declare no competing financial interest.

ACKNOWLEDGMENTS

This work was supported in part by the National Science Foundation Award # DMR-2122078, NASA Awards # 80NSSC19M0201, and Department of Defense Awards # W911NF2210186 and W911NF2310152. The authors thank Bharavi Misra and Dr. Joshua Stapleton at the Pennsylvania State University for TEM access. R.P.-R. acknowledges support from the NASA Graduate Fellowship Award # 80NSSC20K1462.

REFERENCES

(1) Mariotti, N.; Bonomo, M.; Fagiolari, L.; Barbero, N.; Gerbaldi, C.; Bella, F.; Barolo, C. Recent advances in eco-friendly and cost-effective materials towards sustainable dye-sensitized solar cells. *Green Chem.* **2020**, *22* (21), 7168−7218.

(2) Wu, J.; Lan, Z.; Lin, J.; Huang, M.; Huang, Y.; Fan, L.; Luo, G.; Lin, Y.; Xie, Y.; Wei, Y. Counter electrodes in dye-sensitized solar cells. *Chem. Soc. Rev.* **2017**, *46* (19), 5975−6023.

(3) Kakiage, K.; Aoyama, Y.; Yano, T.; Oya, K.; Fujisawa, J.-I.; Hanaya, M. Highly-efficient dye-sensitized solar cells with collaborative sensitization by silyl-anchor and carboxy-anchor dyes. *Chem. Commun.* **2015**, *51* (88), 15894−15897.

(4) Kang, G.; Choi, J.; Park, T. Pt-Free Counter Electrodes with Carbon Black and 3D Network Epoxy Polymer Composites. *Sci. Rep.* **2016**, *6* (1), No. 22987.

(5) Mposa, E.; Sithole, R. K.; Ndala, Z.; Ngubeni, G. N.; Mubiayi, K. P.; Shumbula, P. M.; Machogo-Phao, L. F. E.; Moloto, N. Novel 2D-AuSe nanostructures as effective platinum replacement counter electrodes in dye-sensitized solar cells. *RSC Adv.* **2022**, *12* (20), 12882−12890.

(6) Venkatesan, S.; Chuang, I.-T.; Teng, H.; Lee, Y.-L. High-Performance Carbon Black-Based Counter Electrodes for Copper (I)/(II)-Mediated Dye-Sensitized Solar Cells. *ACS Sustainable Chem. Eng.* **2023**, *11* (32), 12166−12176.

(7) Duerto, I.; Carrera, C.; Barrios, D.; Benito, A. M.; Maser, W. K.; Villacampa, B.; García-Bordejé, E.; Blesa, M.-J. Metal-Free Counter Electrodes for DSSCs Based on Nitrogen-Doped Reduced Graphene Oxide Materials. *Colorants* **2023**, *2* (2), 443−452.

(8) Sheela, S. E.; Sekar, R.; Maurya, D. K.; Paulraj, M.; Angaiah, S. Progress in transition metal chalcogenides-based counter electrode materials for dye-sensitized solar cells. *Mater. Sci. Semicond. Process.* **2023**, *156*, No. 107273, DOI: 10.1016/j.mssp.2022.107273.

(9) Zhao, H.; Nie, F.; Liu, S.; Li, Y.; Wu, K.; Wu, M. Hierarchical α-MoC1-@N-doped carbon nanospheres as counter electrodes for dye-sensitized solar cells. *Diamond Relat. Mater.* **2023**, *138*, No. 110200.

(10) Liu, Sa.; Wang, S.; Wang, Z.; Qi, W.; Guo, H.; Liu, Y.; Luo, Y.; Zhang, W.; Li, L. Synthesis of carbon nanofibers supported NiMoO4 nanoparticles composites used for liquid thin film solar cells counter electrode. *Int. J. Hydrogen Energy* **2023**, *48*, No. 31187.

(11) Meng, Y.; Wang, W.; Zhang, C.; Yao, J.; Xie, C.; Zi, Z.; Lin, C.; Lu, S.; Li, G. Synergistic NiO/Fe2O3 heterostructure-enhanced electrocatalytic performance in dye-sensitized solar cells. *CrystEngComm* **2023**, *25* (30), 4290−4298.

(12) Mutta, G. R.; Popuri, S. R.; Maciejczyk, M.; Robertson, N.; Vasundhara, M.; Wilson, J. I. B.; Bennett, N. S. V2O5as an inexpensive counter electrode for dye sensitized solar cells. *Mater. Res. Express* **2016**, *3* (3), No. 035501, DOI: 10.1088/2053-1591/3/3/035501.

(13) Kurokawa, Y.; Kato, T.; Pandey, S. S. Controlling the electrocatalytic activities of conducting polymer thin films toward suitability as cost-effective counter electrodes of dye-sensitized solar cells. *Synth. Met.* **2023**, *296*, No. 117362, DOI: 10.1016/j.synthmet.2023.117362.

(14) Saranya, K.; Rameez, M.; Subramania, A. Developments in conducting polymer based counter electrodes for dye-sensitized solar cells − An overview. *Eur. Polym. J.* **2015**, *66*, 207−227.

(15) Mohammadnezhad, M.; Selopal, G. S.; Alsayyari, N.; Akilimali, R.; Navarro-Pardo, F.; Wang, Z. M.; Stansfield, B.; Zhao, H.; Rosei, F. J. CuS/graphene nanocomposite as a transparent conducting oxide and pt-free counter electrode for dye-sensitized solar cells. *Chempluschem* **2018**, *83* (5), No. H3065, DOI: 10.1002/cplu.201800046.

(16) Mohammadnezhad, M.; Liu, M.; Selopal, G. S.; Navarro-Pardo, F.; Wang, Z. M.; Stansfield, B.; Zhao, H.; Lai, C.-Y.; Radu, D. R.; Rosei, F. Synthesis of highly efficient Cu2ZnSnSxSe4−x (CZTSSe) nanosheet electrocatalyst for dye-sensitized solar cells. *Electrochim. Acta* **2020**, *340*, No. 135954.

(17) Prado-Rivera, R.; Chang, C. Y.; Liu, M.; Lai, C. Y.; Radu, D. R. Sulvanites: The Promise at the Nanoscale. *Nanomaterials* **2021**, *11* (3), 823.

(18) Woods-Robinson, R.; Han, Y.; Zhang, H.; Ablekim, T.; Khan, I.; Persson, K. A.; Zakutayev, A. Wide Band Gap Chalcogenide Semiconductors. *Chem. Rev.* **2020**, *120* (9), 4007−4055.

(19) Li, Y.; Wu, M.; Zhang, T.; Qi, X.; Ming, G.; Wang, G.; Quan, X.; Yang, D. Natural sulvanite Cu3MX4 (M = Nb, Ta; X = S, Se): Promising visible-light photocatalysts for water splitting. *Comput. Mater. Sci.* **2019**, *165*, 137−143.

(20) Arribart, H.; Sapoval, B.; Gorochov, O.; LeNagard, N. Fast ion transport at room temperature in the mixed conductor Cu3VS4. *Solid State Commun.* **1978**, *26* (7), 435−439.

(21) Syu, W.-J.; Hsu, R.-Y.; Lin, Y.-C. Growth and photovoltaic device using Cu3VS4 films prepared via co-sputtering from Cu−V and V targets. *Mater. Chem. Phys.* **2022**, *277*, No. 125547, DOI: 10.1016/j.matchemphys.2021.125547.

(22) Ikeda, S.; Aono, N.; Iwase, A.; Kobayashi, H.; Kudo, A. Cu3MS4 (M=V, Nb, Ta) and its Solid Solutions with Sulvanite Structure for Photocatalytic and Photoelectrochemical H2 Evolution under Visible-Light Irradiation. *ChemSusChem* **2019**, *12* (9), 1977−1983.

(23) Zhai, X. P.; Ma, B.; Xiao, M. J.; Shang, W.; Zeng, Z. C.; Wang, Q.; Zhang, H. L. Flexible optical limiters based on Cu3VSe4 nanocrystals. *Nanoscale* **2023**, *15*, No. 10606.

(24) Fukai, H.; Nagatsuka, K.; Yamaguchi, Y.; Iwase, A.; Kudo, A. Powder-Based Cu3VS4 Photocathode Prepared by Particle-Transfer Method for Water Splitting Using the Whole Range of Visible Light. *ECS J. Solid State Sci. Technol.* **2022**, *11* (6), No. 063002.

(25) Wu, M.; Li, Q. F.; Cheng, S. L.; Yao, K. T.; Liu, L.; Jiang, Y.; Feng, Y. Z.; Rui, X. H.; Yu, Y. Cu-V bimetallic selenide with synergistic effect for high-rate and long-life sodium storage. *J. Mater. Res.* **2022**, *37*, 3308−3317, DOI: 10.1557/s43578-022-00623-0.

(26) Chen, D.; Miao, X. W.; Liu, J.; Zhang, L.; Dai, Z. F.; Dong, H. L.; Yang, J.; Geng, H. B. Microspherical copper tetrathiovanadate with stable binding site as ultra-rate and extended longevity anode for sodium-ion half/full batteries. *Chem. Eng. J.* **2022**, *446*, No. 136772, DOI: 10.1016/j.cej.2022.136772.

(27) Li, Q.; Ye, X.; Cheng, S.; Yu, H.; Liu, W.; Du, C.-F.; Rui, X. A copper tetrathiovanadate anode for ultra-stable potassium-ion storage. *Mater. Chem. Front.* **2021**, *6* (1), 63−70.

(28) Kehoe, A. B.; Scanlon, D. O.; Watson, G. W. The electronic structure of sulvanite structured semiconductors Cu3MCh4(M = V, Nb, Ta; Ch = S, Se, Te): prospects for optoelectronic applications. *J. Mater. Chem. C* **2015**, *3* (47), 12236−12244.

(29) Kehoe, A. B.; Scanlon, D. O.; Watson, G. W. Modelling potential photovoltaic absorbers Cu3MCh4(M = V, Nb, Ta; Ch = S, Se, Te) using density functional theory. *J. Phys.: Condens. Matter* **2016**, *28* (17), No. 175801.

(30) Espinosa-García, W.; Valencia-Balvín, C.; Osorio-Guillén, J. M. Phononic and thermodynamic properties of the sulvanite compounds: A first-principles study. *Comput. Mater. Sci.* **2016**, *113*, 275−279.

(31) Peralta, J.; Valencia-Balvín, C. Vibrational properties of Cu3XY4 sulvanites (X = Nb, Ta, and V; and Y = S, and Se) by ab initio molecular dynamics. *Eur. Phys. J. B* **2017**, *90* (9), No. 177, DOI: 10.1140/epjb/e2017-80050-7.

(32) Chen, E. M.; Stoyko, S. S.; Aitken, J. A.; Poudeu, P. F. P. Tuning the optical, electronic and thermal properties of Cu3NbS4-xSex through chemical substitution. *Inorg. Chem. Front.* **2017**, *4* (9), 1493−1500.

(33) Grima-Gallardo, P.; Salas, M.; Contreras, O.; Power, C.; Quintero, M.; Cabrera, H.; Zumeta-Dube, I.; Rodriguez, A.; Aitken, J.; Bramer-Escamilla, W. Cu3TaSe4 and Cu3NbSe4: X-ray diffraction, differential thermal analysis, optical absorption and Raman scattering. *J. Alloys Compd.* **2016**, *658*, 749−756.

(34) Chen, C. C.; Stone, K. H.; Lai, C. Y.; Dobson, K. D.; Radu, D. Sulvanite (Cu3VS4) nanocrystals for printable thin film photovoltaics. *Mater. Lett.* **2018**, *211*, 179−182.

https://doi.org/10.1021/acsami.3c18658
ACS Appl. Mater. Interfaces 2024, 16, 13719−13728

(35) Rao, C. N. R.; Kulkarni, G. U.; Thomas, P. J.; Edwards, P. P. Size-Dependent Chemistry: Properties of Nanocrystals. *Chem.- Eur. J.* **2002**, *8* (1), 28−35.
(36) Mantella, V.; Ninova, S.; Saris, S.; Loiudice, A.; Aschauer, U.; Buonsanti, R. Synthesis and Size-Dependent Optical Properties of Intermediate Band Gap Cu3VS4 Nanocrystals. *Chem. Mater.* **2019**, *31* (2), 532−540.
(37) Liu, M. M.; Lai, C. Y.; Chang, C. Y.; Radu, D. R. Solution-Based Synthesis of Sulvanite Cu3TaS4 and Cu3TaSe4 Nanocrystals. *Crystals* **2021**, *11* (1), 51.
(38) Liu, M.; Lai, C. Y.; Zhang, M.; Radu, D. R. Cascade synthesis and optoelectronic applications of intermediate bandgap Cu3VSe4 nanosheets. *Sci. Rep.* **2020**, *10* (1), No. 21679.
(39) Cao, J. M.; Ma, M. Y.; Liu, H. H.; Yang, J. L.; Liu, Y.; Zhang, K. Y.; Butt, F. A.; Gu, Z. Y.; Li, K.; Wu, X. L. Interfacial-Confined Isochronous Conversion to Biphasic Selenide Heterostructure with Enhanced Adsorption Behaviors for Robust High-Rate Na-Ion Storage. *Small* **2024**, No. 2311024, DOI: 10.1002/smll.202311024.
(40) Liu, M.; Lai, C. Y.; Selopal, G. S.; Radu, D. R. Synthesis and optoelectronic properties of Cu3VSe4 nanocrystals. *PLoS One* **2020**, *15* (5), No. e0232184.
(41) Kaur, N.; Oyon, S. A.; Lai, C.-Y.; Radu, D. R. From reflection to absorption: Improving light harvesting of dye sensitized solar cells with Cu nanowires as reflectors. *Opt. Mater.* **2023**, *142*, No. 114074.
(42) Kaur, N.; Syed, F. M.; Fina, J.; Lai, C.-Y.; Radu, D. R. Ag Reflectors: An Effective Approach to Improve Light Harvesting in Dye Sensitized Solar Cells. *IEEE J. Photovoltaics* **2023**, *13* (2), 250−253.
(43) Fina, J.; Kaur, N.; Chang, C.-Y.; Lai, C.-Y.; Radu, D. R. Enhancing Light Harvesting in Dye-Sensitized Solar Cells through Mesoporous Silica Nanoparticle-Mediated Diffuse Scattering Back Reflectors. *Electron. Mater.* **2023**, *4*, 124−135.
(44) Kaur, N.; Syed, F. M.; Fina, J.; Lai, C.-Y.; Radu, D. R. Ag Reflectors: An Effective Approach to Improve Light Harvesting in Dye Sensitized Solar Cells. *IEEE J. Photovoltaics* **2023**, *13*, 1−4.
(45) van Embden, J.; Chesman, A. S. R.; Jasieniak, J. J. The Heat-Up Synthesis of Colloidal Nanocrystals. *Chem. Mater.* **2015**, *27* (7), 2246−2285.
(46) Liu, Y.; Ding, T.; Luo, X.; Li, Y. L.; Long, J. L.; Wu, K. F. Tuning Intermediate-Band Cu3VS4 Nanocrystals from Plasmonic-like to Excitonic via Shell-Coating. *Chem. Mater.* **2020**, *32* (1), 224−233.
(47) Chang, C. Y.; Prado-Rivera, R.; Liu, M.; Lai, C. Y.; Radu, D. R. Colloidal Synthesis and Photocatalytic Properties of Cu3NbS4 and Cu3NbSe4 Sulvanite Nanocrystals. *ACS Nanosci. Au* **2022**, *2* (5), 440−447.
(48) Walker, B. C.; Agrawal, R. Contamination-free solutions of selenium in amines for nanoparticle synthesis. *Chem. Commun.* **2014**, *50* (61), 8331−8334.
(49) Schmidt, K.; Müller, A.; Bouwma, J.; Jellinek, F. J. Übergangsmetall-chalklogen-verbindungen IR-und raman-spektren von Cu3Mx4 (m= v, nb, ta; x= s, se). *J. Mol. Struct.* **1972**, *11* (2), 275−282, DOI: 10.1016/0022-2860(72)80012-7.
(50) Sarker, S.; Lee, K.-S.; Seo, H. W.; Jin, Y.-K.; Kim, D. M. Reduced graphene oxide for Pt-free counter electrodes of dye-sensitized solar cells. *Sol. Energy* **2017**, *158*, 42−48.
(51) Yue, G.; Cheng, R.; Gao, X.; Fan, L.; Mao, Y.; Gao, Y.; Tan, F. Synthesis of MoIn2S4@CNTs Composite Counter Electrode for Dye-Sensitized Solar Cells. *Nanoscale Res. Lett.* **2020**, *15* (1), No. 179, DOI: 10.1186/s11671-020-03410-0.
(52) Wu, K.; Yang, D.; Guo, J.; Fu, P.; Wu, R.; Zheng, Y.; Wu, M. Performance of V2O3@C composites via a sol−gel precursor assisted by soluble starch as Pt-free counter electrodes for dye sensitized solar cells. *Sol. Energy* **2021**, *213*, 126−135.
(53) Kumar, R.; Sahajwalla, V.; Bhargava, P. J. Fabrication of a counter electrode for dye-sensitized solar cells (DSSCs) using a carbon material produced with the organic ligand 2-methyl-8-hydroxyquinolinol (Mq). *Nanoscale Adv.* **2019**, *1* (8), 3192−3199, DOI: 10.1039/C9NA00206E.
(54) Dong, A.; Ye, X.; Chen, J.; Kang, Y.; Gordon, T.; Kikkawa, J. M.; Murray, C. B. A Generalized Ligand-Exchange Strategy Enabling Sequential Surface Functionalization of Colloidal Nanocrystals. *J. Am. Chem. Soc.* **2011**, *133* (4), 998−1006.
(55) Wheeler, L. M.; Sanehira, E. M.; Marshall, A. R.; Schulz, P.; Suri, M.; Anderson, N. C.; Christians, J. A.; Nordlund, D.; Sokaras, D.; Kroll, T.; et al. Targeted Ligand-Exchange Chemistry on Cesium Lead Halide Perovskite Quantum Dots for High-Efficiency Photovoltaics. *J. Am. Chem. Soc.* **2018**, *140* (33), 10504−10513.
(56) Chou, J.-C.; Ko, C.-C.; Chang, J.-X.; Lai, C.-H.; Nien, Y.-H.; Kuo, P.-Y.; Chen, H.-H.; Hsu, H.-H.; Hu, G.-M. Dye-sensitized solar cells using aluminum-doped zinc oxide/titanium dioxide photoanodes in parallel. *Energies* **2019**, *12* (18), No. 3469, DOI: 10.3390/en12183469.
(57) Ju, M. J.; Jeon, I.-Y.; Kim, H. M.; Choi, J. I.; Jung, S.-M.; Seo, J.-M.; Choi, I. T.; Kang, S. H.; Kim, H. S.; Noh, M. J. Edge-selenated graphene nanoplatelets as durable metal-free catalysts for iodine reduction reaction in dye-sensitized solar cells. *Sci. Adv.* **2016**, *2* (6), No. e1501459, DOI: 10.1126/sciadv.1501459.